

Complex Precipitates of TiN-MC_x in GCr15 Bearing Steel

Qianren Tian¹, Guocheng Wang^{1,2,3)*}, Xinghu Yuan¹, Qi Wang^{1,2}, and Seetharaman Sridhar³

1. School of Materials and Metallurgy, University of Science and Technology Liaoning, Anshan, Liaoning, 114051 P. R China.

2. Key Laboratory of Chemical Metallurgy Engineering Liaoning Province, University of Science and Technology Liaoning, Anshan, Liaoning, 114051 P. R China.

3. Department of Metallurgical and Materials Engineering, Colorado school of mines, Golden, CO, 80401 USA.

*Corresponding Author: GUOCHENG WANG

Email Address: wang_guocheng@163.com

ABSTRACT

Nitride and carbide are the second phases which play an important role in the performance of bearing steel, and their precipitation behavior is complicated. In this study, TiN-MC_x precipitations in GCr15 bearing steels were obtained by non-aqueous electrolysis, and their precipitation mechanisms were studied. TiN is the effective heterogeneous nucleation site for Fe₇C₃ and Fe₃C, therefore, MC_x can precipitate on the surface of TiN easily, its chemistry component consists of M₃C and M₇C₃ (M = Fe, Cr, Mn) and Cr₃C₂. TiN-MC_x with high TiN volume fraction, TiN forms in early stage of solidification, and MC_x precipitates on TiN surface after TiN engulfed by the solidification advancing front. TiN-MC_x with low TiN volume fraction, TiN and MC_x form in late stage of solidification, TiN can not grow sufficiently and is covered by a large number of precipitated MC_x particles.

KEYWORDS: Non-aqueous electrolysis, TiN-MC_x, Precipitation, High carbon chromium bearing steel

1. INTRODUCTION

Controlling microstructures and second phase in steel plays an vital role in the quality of steel. Carbide (M_3C , M_3C_2 , M_7C_3 , $M = Fe, Cr, Mn$)[1,2] and TiN inclusion[3,4] are common second phase in high carbon chromium steel. Due to the good wear resistance and solid solubility with alloy elements (Cr, Mn)[5,6], carbide can keep good mechanical properties of bearing steel during heat treatment[7,8]. In recent years, utilization of inclusions has become attractive to improve steel performance. TiN is more harmful to bearing steel than Al_2O_3 in the same size[9]. Many studies have investigated TiN and Al_2O_3 , $MgAl_2O_4$ and MnS, and NbC complex precipitation with inclusion[10-13]. Our previous study[14] found that TiN inclusion were covered by carbide in the etched GCr15 bearing steel metallographic specimens. Considering the two-dimensional (2-D) of particles cannot reflect their real morphologies, it is necessary to observe their three-dimensional (3-D) morphologies in steel.

The non-aqueous electrolysis extraction of second phase from steel is an effective method to study their 3-D morphologies and composite interfaces. Fang et al.[15] studied the behaviors of rare earth dissolved in α -Fe, Fe-Ce intermetallic compounds and rare earth inclusions via non-aqueous electrolysis. Bi et al.[16] analyzed 3-D morphology, quantity and chemistry of inclusion in ferroalloys by the electrolysis method. Wang et al.[17] observed Al_2O_3 -MnO-SiO₂(-MnS) inclusion in steel by non-aqueous electrolysis. X. W. Zhang et al.[18,19] analyzed Ca-Mg spinel in cord steel and MnS in heavy rail steel by the electrolysis. D. Zhang et al.[20] studied the suitable electrolytic conditions for 16MnCrS5 steel.

In this study, 3-D morphologies of the carbide (MC_x , $M = Fe, Cr, Mn$) and TiN- MC_x precipitates extracted from GCr15 bearing steel specimens by the non-aqueous electrolysis were observed by field emission scanning electron microscope - energy dispersive spectrometer (FESEM - EDS). The MC_x chemistry component was confirmed by X-ray diffraction (XRD) and FactSageTM phase diagram calculation. The precipitation mechanism of TiN- MC_x with different volume fraction in GCr15 bearing steels was elucidated.

2. EXPERIMENTAL

2.1 CHEMICAL COMPONENTS ANALYSIS

The chemical compositions of GCr15 bearing steel produced by the basic oxygen furnace (BOF)-ladle furnace (LF)-vacuum degas (VD)-continuous casting (CC) process in a foundry were determined by direct-reading spectrometer (Model: ARL-3460 Optical Emission Spectrometer, Thermo Fisher Corporation).

The total oxygen and total nitrogen contents were analyzed using a nitrogen-oxygen analyzer (Model: TC-600, LECO Corporation). The chemical compositions of the GCr15 bearing steel are shown in **Table 1**.

Table 1. Chemical Compositions of GCr15 Bearing Steel (in mass percent)

| Composition | C | Si | Mn | P | S | Ti | Cr | V | N | Alt | Ca | O(T) |
|---------------|------|------|------|-------|--------|--------|------|--------|--------|-------|--------|--------|
| Concentration | 1.01 | 0.25 | 0.36 | 0.012 | 0.0014 | 0.0078 | 1.46 | 0.0099 | 0.0049 | 0.012 | <0.005 | 0.0009 |

2.2 NON-AQUEOUS ELECTROLYSIS AND XRD DETECTION

The non-aqueous electrolysis method was used to extract TiN-MC_x particles from the GCr15 bearing steel. Samples with diameter of 10 mm and height of 100 mm were as anode and copper as cathode. The electrolyte consists of 1% tetramethylammonium chloride, 5% triethanolamine, 5% glycerol, and 89% anhydrous methanol (in volume percentage). The constant voltage DC power supply (model: DH1720A-1) was used to keep the current density between 40 - 60 mA/cm². The temperature of the electrolyte was kept at 268 - 278 K (- 5 - 5 °C). Argon gas was used to stir organic electrolyte. After electrolysis, steel samples were placed to a beaker containing ethanol and vibrated with ultrasonic wave to separate all particles from the samples surface. MC_x and inclusions in ethanol were further separated by the magnetism. The inclusion particles were transferred directly to the double-sided carbon bands attached to the conductive material, and then were observed by FESEM-EDS. After magnetic separation, MC_x was analyzed by XRD (Model: X'Pert Powder, Malvern PANalytic Ltd.).

3. RESULT

3.1 OBSERVATION FOR PARTICLES

2-D morphologies of TiN-MC_x in the metallographic specimens etched by 4% nitric acid alcohol are observed by FESEM-EDS and shown in **Figure 1**. The dark grey particles are TiN inclusions, and the light grey particles are MC_x. **Figure 1(a)** shows a long strip and large size TiN with a small amount of MC_x around it. **Figures 1(b) to (d)** show TiN with less pronounced aspect ratios and its covered by a larger number of MC_x, which in some cases form a continuous layer rather than discrete particles.

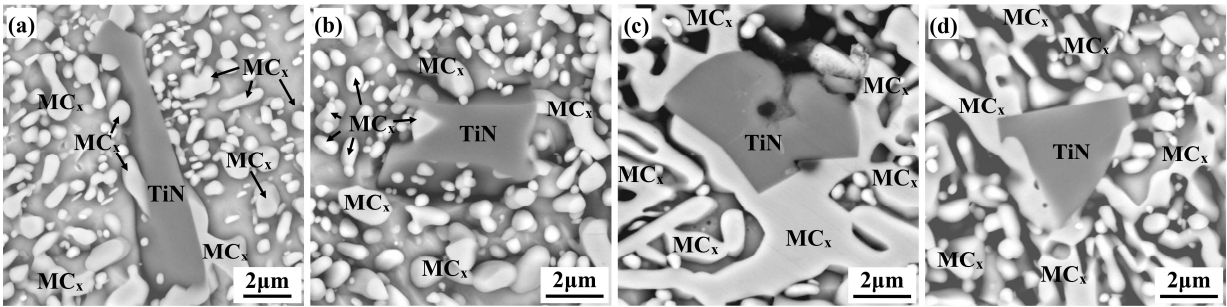


Figure 1 TiN-MC_x particles in etched metallographic specimens. (a) long-strip and large size TiN with MC_x; (b) - (d) small size TiN with MC_x.

3-D morphologies and chemistries of TiN-MC_x were also observed by FESEM-EDS. **Figure 2(a)** shows TiN-MC_x with large size TiN inclusion (in comparison to MC_x) whose size is approximately 25 μm. This category of TiN-MC_x is denoted as “TiN-MC_x with high TiN volume fraction” in this paper. The elements mapping shows that Ti and V can form the solid solution, while the metallic elements in MC_x are Fe and Cr, Mn can not be detected because of its low content. **Figure 2(b)** shows that TiN-MC_x with small size TiN are approximately 5 μm, its shape is closer to a sphere. Compared with the TiN-MC_x in **Figures 2(a)**, TiN in the precipitates is clearly smaller. This category of TiN-MC_x is denoted as “TiN-MC_x with low TiN volume fraction”. The TiN-MC_x with low TiN volume fraction is almost completely covered by MC_x.

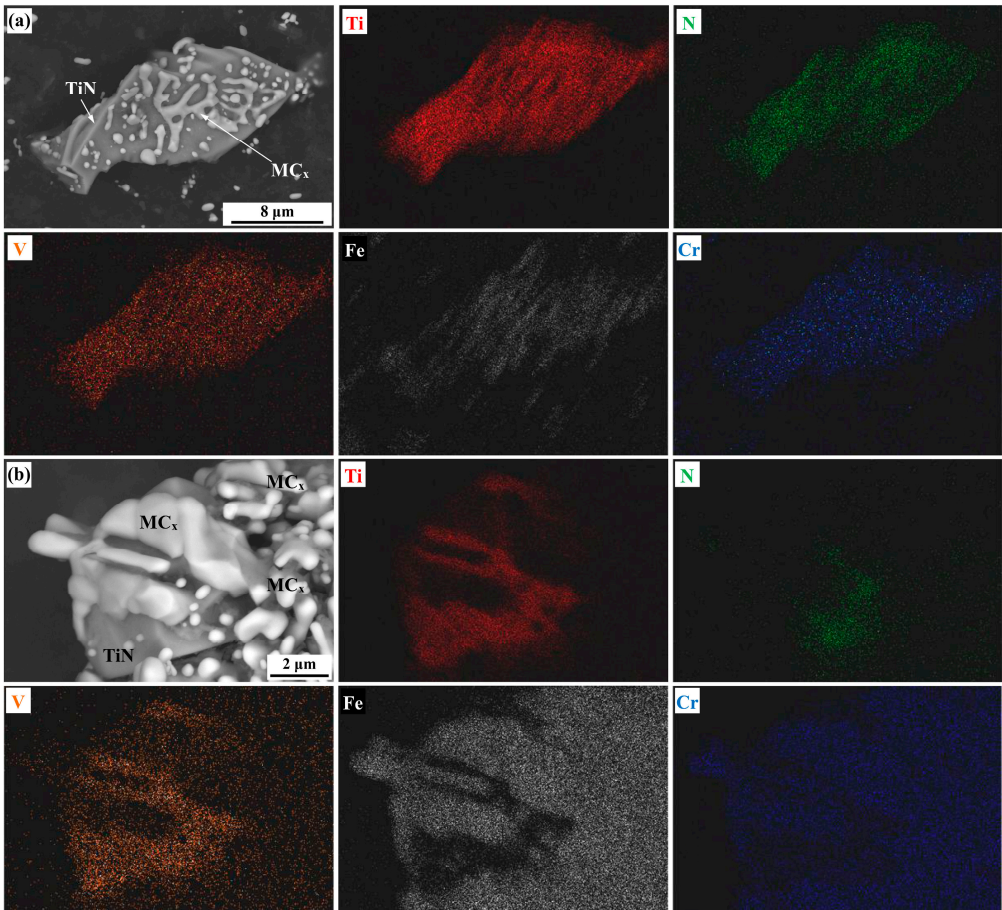


Figure 2 Morphologies and elements mapping of TiN-MC_x. (a) high TiN volume fraction; (b) low TiN volume fraction.

Figure 3 shows the 3-D morphologies of MC_x and elements mapping of Fe, Cr, and Mn. The morphologies of single MC_x particles are not significantly different from that of MC_x on the surface of TiN inclusion. **Figure 3(a)** shows a spherical MC_x with a smaller size less 1 μm. **Figure 3(b)** shows a flat MC_x with approximate 1 μm whereas a MC_x with a shape of a long strip of length 6 μm in **Figure 3(c)**, which is rarely found in steel. **Figure 3(d)** shows MC_x transferred on the conductive carrier, and the MC_x are predominantly spherical and flat. **Figures 3(e)** and (f) are cluster-like MC_x with Fe, Cr and Mn elements mapping results. The size of cluster-like MC_x are approximately 15 μm. However, the cluster-like MC_x exhibits the morphology of banded or reticulated MC_x in metallographic samples. In **Figures 3(e)** and (f), C is not shown since MC_x and inclusions were transferred on the carbon bands.

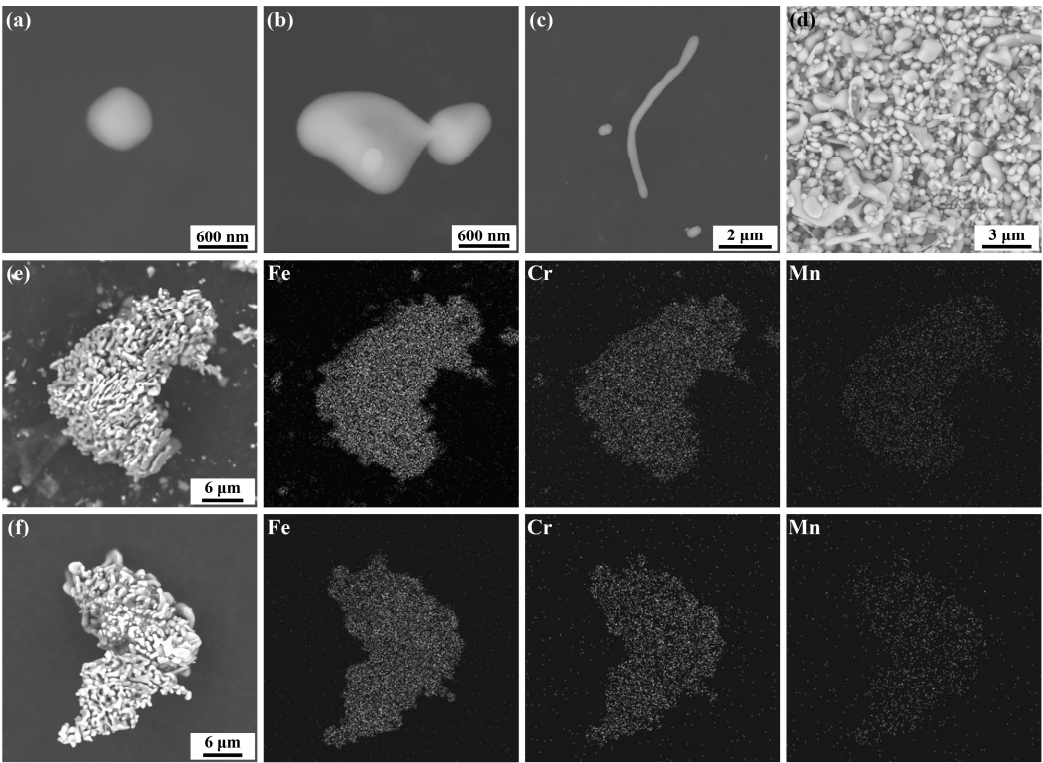


Figure 3 Morphologies and elements mapping of MC_x. (a) ball-like MC_x; (b) flat-like MC_x; (c) long stripe-like; (d) MC_x transferred on the conductive carrier; (e) and (f) cluster-like MC_x with elements mapping of Fe, Cr, and Mn.

3.2 XRD RESULT

Figure 4 shows the result of MC_x XRD experiment, the structure of MC_x are predominantly M₃C and M₇C₃, with M₃C being the dominant carbide. At 2θ = 48.6 °, there are a few Cr₃C₂. The results are similar to carbides in GCr15 bearing steel after electroslag remelting-continuous casting (ESR-CC) process by Du et al.[2] The main MC_x in that study were M₃C, M₃C₂ and M₇C₃, and the content of Cr in their sample was 1.47% and 0.31%[2], respectively, which is similar to that in our steel.

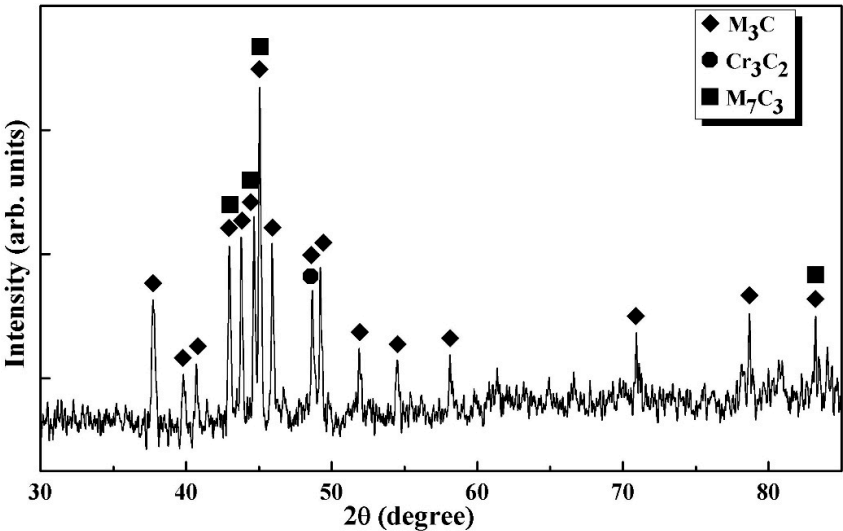


Figure 4 XRD analysis result of the extracted MC_x in the GCr15 bearing steel.

4. DISCUSSION

4.1 THERMODYNAMIC ANALYSIS

The phase diagram of Fe-1.5%Cr-C system was calculated by using the FactSage™ 7.2 thermodynamic software and steel database[21]. The calculated phase diagram for the conditions, [pct Cr] = 1.5, [pct C] = 0.5 - 1.5 ([pct element] is mass percent of the element in steel), and the temperature range from 298 K (25 °C) to 1873 K (1600 °C), is shown in **Figure 5** and the gray part presents the mushy zone of steel. When [pct C] = 1, equilibrium transformation of steel is that liquid → FCC + liquid → FCC → M₃C + FCC → M₃C + FCC + BCC → M₃C + BCC → C + M₃C + BCC → C + BCC + M₇C₃ → C + BCC + Cr₃C₂. The liquidus temperature and solidus temperature are close to the calculated values in our previous paper [liquidus and solidus temperature are 1723 K (1450 °C) and 1601 K (1328 °C), respectively][14]. When the temperature is slightly lower than 1173 K (900 °C), M₃C gradually precipitates from FCC phase; when the temperature is approximately 913 K (640 °C), M₃C gradually transforms to M₇C₃; and when the temperature is slightly higher than 773 K (500 °C), the carbide gradually transforms into Cr₃C₂. In the actual process, phase transformation will be difficult to be completed to the phase fraction dictated by the equilibrium phase diagram which leads to the transition layers. The main phases formed during temperature gradual decreasing are M₃C, M₇C₃, Cr₃C₂, and their content decreases in turn. FactSage™ calculation results are consistent with XRD result, in which MC_x are found to be M₃C, M₇C₃ and Cr₃C₂.

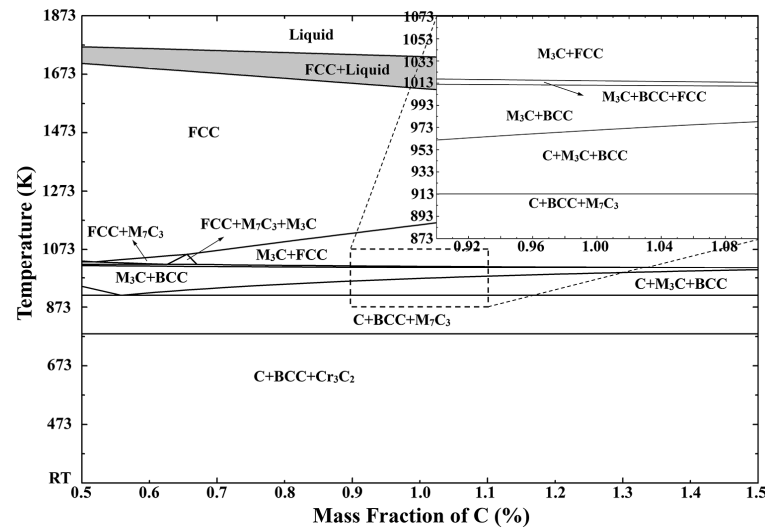


Figure 5 Phase diagram for Fe-1.5%Cr-C system (the shadow part is the mushy zone of steel, C presents the pure substance C(s); M_3C (Cementite) presents Fe_3C with dissolved Cr, Mn; M_7C_3 presents carbide phase found in Cr, Mn-containing steels; FCC and BCC present the face-centered cubic iron (γ -Fe) and body-centered cubic iron (α -Fe), respectively).

According to the authors previous work[14,22], TiN precipitates in the mushy zone of GCr15 bearing steel, and their size is affected by the concentration of Ti and N around TiN crystal nucleus. Ti and N both are positive segregation elements ($k > 0$), their concentrations and consequently the supersaturation increases with solid fraction increasing, and TiN precipitation become easier during solidification process.

Fe, Cr, Mn, and C can precipitate on TiN, which is the heterogeneous nucleation site for MC_x . It is seen in **Figure 2(a)** that the size of TiN is large and consequently, TiN would be formed at the early stage of solidification, and has enough time to growth. TiN in **Figure 2(b)** precipitates at the late stage of solidification. The diffusion coefficients D_i , $i = Cr, Ti, Mn, C, N$ in γ -phase were calculated according to the phase diagrams, when $[pct C] = 1$ and FCC precipitates at 1673 K (1400 °C). The relationship between diffusion coefficients and temperature from 1673 to 1173 K (1400 to 900 °C) is shown in **Figure 6(a)**, and the parameters are shown in **Table 2**. From **Figure 6(a)**, in 1673 - 1642 K (1400 - 1369 °C), $D_N^\gamma > D_C^\gamma > D_{Ti}^\gamma > D_{Mn}^\gamma > D_{Cr}^\gamma$; in 1642 - 1173 K (1369 - 900 °C), $D_C^\gamma > D_N^\gamma > D_{Ti}^\gamma > D_{Mn}^\gamma > D_{Cr}^\gamma$. The results indicate that the diffusion of C and N plays a dominant role, the diffusion of C is more efficient than N after the temperature decreased under 1642 K, while the diffusion of Cr, Ti, and Mn are extremely small in γ -phase, the content of Cr is much larger than that of Mn and Ti, this would not affect the precipitation of MC_x . That means that TiN may precipitate more easily

160 in the range of temperature of 1673 K- 1642 K, while MC_x precipitates easily during the following decreasing
161 temperature process.

162

163 **Table 2.** Diffusion Coefficient and Equilibrium Partition Coefficient of C, Cr, Mn, Ti, and N in γ-phase
164 [28~31].

| Element | Equilibrium Partition Coefficient, <i>k</i> | Diffusion Coefficient in γ-phase (cm ² /s) |
|---------|---|---|
| C | 0.34 | 0.0761·EXP(-134600/RT) |
| Cr | 0.85 | 0.0012·EXP(-219000/RT) |
| Mn | 0.78 | 0.486·EXP(-276100/RT) |
| Ti | 0.33 | 0.15·EXP(-251000/RT) |
| N | 0.48 | 0.91·EXP(-168500/RT) |

165

166 The segregation degree of C, Cr, Ti, Mn, and N during solidification is calculated according to Equations
167 (1) to (5)[32], in **Figure 6(b)**, at cooling rate of 0.5 K/s, temperature of 1723 K to 1601 K (1450 °C to
168 1328 °C), corresponding solid fraction is 0~1. The order of segregation from high to low is Ti, C, N, Mn and
169 Cr at the same solid fraction. The segregation degree of C at the late stage of solidification reaches tens of
170 times of the initial content. Therefore, MC_x precipitation on the TiN surface becomes easier at the late stages
171 of solidification.

172
$$\frac{[\text{pct } X]_t}{[\text{pct } X]_0} = \left[1 - \left(1 - \frac{\beta k_i}{1 + \beta} \right) \cdot f_s \right]^{\frac{k_i - 1}{1 - \frac{\beta k_i}{1 + \beta}}} \quad (1)$$

173
$$\beta = \frac{4D_i^\gamma}{L^2} \quad (2)$$

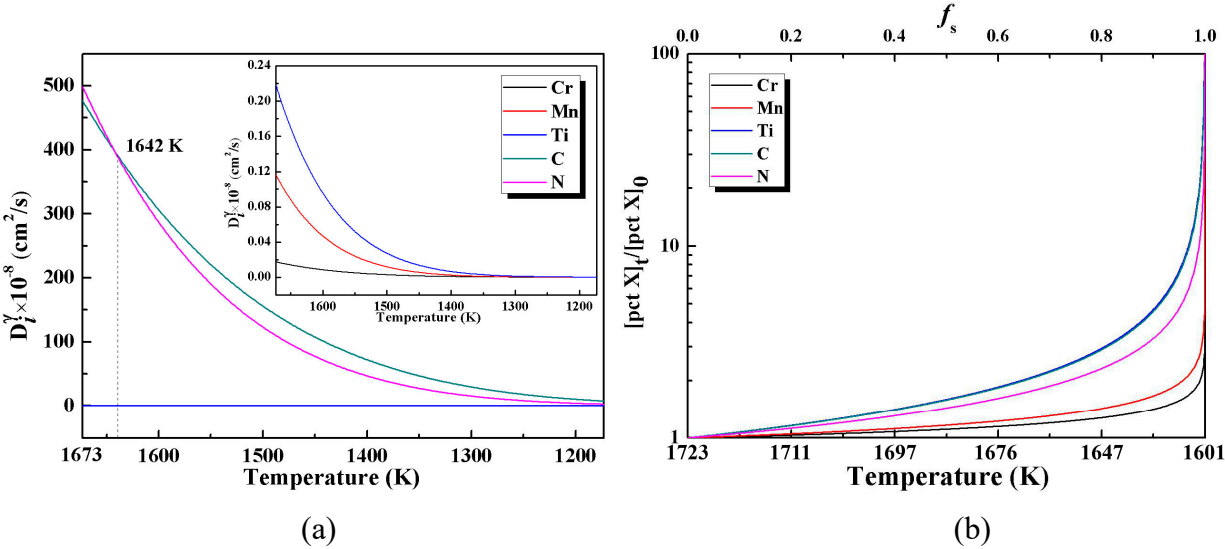
174
$$\tau = \frac{T_l - T_s}{R_c} \quad (3)$$

175
$$L = 143.9 \times R_c^{-0.386}, \quad ([\text{pct } C] = 1) \quad (4)$$

176
$$T = T_{Fe} - \frac{T_{Fe} - T_l}{1 - f_s \frac{T_l - T_s}{T_{Fe} - T_s}} \quad (5)$$

177 Here, [pct X]_t is the C concentration at solidification front, [pct X]₀ is the initial C concentration; *f_s* is solid

178 fraction; k_i is equilibrium distribution coefficient of C, Cr, Mn, Ti, and N in γ -phase; D_i^γ is diffusion
179 coefficient of C, Cr, Mn, Ti, and N in γ -phase, cm^2/s ; τ is the local cooling time, s; R_c is the local cooling rate,
180 K/s; L is secondary arm space, μm ; T_{Fe} , T_l , and T_s are the melting point of pure iron [1809 K (1536 °C)], the
181 liquidus temperature [1723 K (1450 °C)] and the solidus temperature [1601 K (1328 °C)] of GCr15 steel[14],
182 respectively.
183



184
185 (a) (b)
186 **Figure 6** Diffusion coefficient change in γ -phase and segregation degree of C, Mn, Ti, C, N during
187 solidification process (a) diffusion coefficient change; (b) segregation degree.
188

189 **4.2 CRYSTALLOGRAPHIC ANALYSIS**

190 Based on the disregistry theory[23,24], the inconsistency of lattice parameters between matrix and
191 nucleating phase can indicate the effectiveness of nucleating catalysts. Choosing three crystal planes and three
192 crystal orientations of the matrix and new phase crystal, the corresponding crystal parameters can calculate the
193 disregistries between two phases by Equation (6). Since M_3C and M_7C_3 are substitutional solid solutions (Cr
194 and Mn take the position of Fe in carbides)[25], the minimum disregistries of $TiN-M_7C_3$, $TiN-M_3C$, and
195 $Fe_3C-Fe_7C_3$ were verified by the parameters of TiN [14], Fe_7C_3 [26] and Fe_3C [27]. The parameters and
196 calculated results are shown in **Table 3**, and the disregistries diagram is shown in **Figure 7**. The disregistry
197 between $[\bar{1}11] \quad (110)TiN \parallel [\bar{1}11] \quad (110)Fe_7C_3$, $[\bar{1}11] \quad (110)TiN \parallel [\bar{1}11] \quad (110)Fe_3C$ and
198 $[011](100)Fe_3C \parallel [011](100)Fe_7C_3$ are 1.49%, 5.16% and 7.40%, respectively. The results show that the

disregistries between TiN and Fe₇C₃ and Fe₃C are both small, and consequently TiN would provide suitable heterogeneous nucleation sites for Fe₇C₃ and Fe₃C.

$$\delta_{(hkl)_n}^{(hkl)_s} = \frac{1}{3} \sum_{i=1}^3 \frac{|(d_{[uvw]_s}^i \cdot \cos \theta) - d_{[uvw]_n}^i|}{d_{[uvw]_n}^i} \times 100\% \tag{6}$$

where $\delta_{(hkl)_n}^{(hkl)_s}$ is disregistry between a solid plane $(hkl)_s$ and a nucleate plane $(hkl)_n$; $d_{[uvw]_s}^i$ and $d_{[uvw]_n}^i$ are the interatomic spacing along a low-index direction $[uvw]_s$ and the interatomic spacing along a low-index direction $[uvw]_n$; θ is the angle between $[uvw]_s$ and $[uvw]_n$.

Table 3. Parameters and Lattice Disregistry between TiN and Nucleation Phase.

| Substance (space group) | Lattice parameters (length unit: Å) | | | | | |
|--|-------------------------------------|--------------------|--------------------------------|---------------------------------|--------|-------------|
| | a | b | C | $\alpha=\beta=\gamma(^{\circ})$ | | |
| Fe ₇ C ₃ (Pnma) ^[26] | 4.537 | 6.892 | 11.913 | 90 | | |
| TiN-Fe ₇ C ₃ (100)TiN (100)Fe ₇ C ₃ (110)TiN (110)Fe ₇ C ₃ (111)TiN (111)Fe ₇ C ₃ | [hkl] _s | [hkl] _n | d _{[hkl]_s} | d _{[hkl]_n} | θ(°) | Disregistry |
| | [001] | [001] | 2.118 | 11.913 | 0(-) | |
| | [011] | [011] | 2.995 | 13.763 | 14.949 | 6.52% |
| | [010] | [010] | 2.118 | 6.892 | - | |
| | [110] | [001] | 2.995 | 11.913 | - | |
| | [111] | [111] | 3.668 | 14.492 | 0.556 | 1.49% |
| | [001] | [110] | 2.118 | 8.251 | - | |
| | [011] | [011] | 2.995 | 13.763 | 5.275 | |
| | [101] | [101] | 2.995 | 12.748 | 18.715 | 8.93% |
| | [110] | [110] | 2.995 | 8.251 | - | |
| Substance (space group) | Lattice parameters (length unit: Å) | | | | | |
| | a | b | C | $\alpha=\beta=\gamma(^{\circ})$ | | |
| Fe ₃ C (Pnma) ^[27] | 5.092 | 6.741 | 4.527 | 90 | | |

| TiN-Fe ₃ C | [hkl] _s | [hkl] _n | d _{[hkl]_s} | d _{[hkl]_n} | θ(°) | Disregistry |
|---|--------------------|--------------------|--------------------------------|--------------------------------|--------|-------------|
| (100)TiN (100)Fe ₃ C | [001] | [001] | 2.118 | 4.527 | - | |
| | [011] | [011] | 2.995 | 8.120 | 11.116 | 6.92% |
| | [010] | [010] | 2.118 | 6.741 | - | |
| (110)TiN (110)Fe ₃ C | $\bar{1}10$ | $\bar{1}10$ | 2.995 | 8.448 | - | |
| | $\bar{1}11$ | $\bar{1}11$ | 3.668 | 9.585 | 26.551 | 5.16% |
| | [001] | [001] | 2.118 | 4.527 | - | |
| (111)TiN (111)Fe ₃ C | $0\bar{1}1$ | $0\bar{1}1$ | 2.995 | 8.448 | 3.227 | |
| | $\bar{1}01$ | $\bar{1}01$ | 2.995 | 8.120 | 8.258 | 9.25% |
| | $\bar{1}10$ | $\bar{1}10$ | 2.955 | 6.813 | - | |
| Fe ₃ C-Fe ₇ C ₃ | [hkl] _s | [hkl] _n | d _{[hkl]_s} | d _{[hkl]_n} | θ(°) | Disregistry |
| (110)Fe ₃ C (110)Fe ₇ C ₃ | [001] | [001] | 4.527 | 11.913 | - | |
| | $\bar{1}11$ | $\bar{1}11$ | 9.585 | 14.492 | 27.107 | 11.38% |
| | $\bar{1}10$ | $\bar{1}10$ | 8.448 | 8.251 | - | |
| (100)Fe ₃ C (100)Fe ₇ C ₃ | [001] | [001] | 4.527 | 11.913 | - | - |
| | [011] | [011] | 8.120 | 13.763 | 26.068 | 7.40% |
| | [010] | [010] | 6.741 | 6.892 | - | - |
| (111)FeC ₃ (111)Fe ₇ C ₃ | $\bar{1}01$ | $0\bar{1}1$ | 8.120 | 13.763 | 2.983 | |
| | $0\bar{1}1$ | $\bar{1}01$ | 8.448 | 12.748 | 15.488 | 21.0% |
| | $\bar{1}10$ | $\bar{1}10$ | 6.813 | 8.251 | - | |

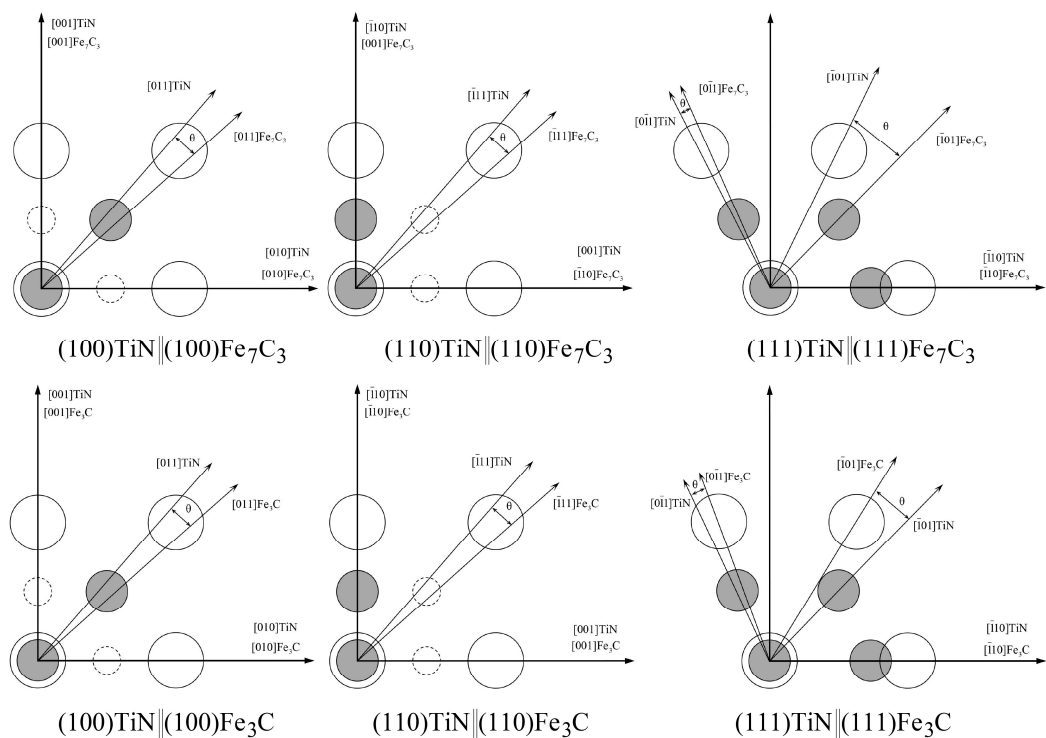


Figure 7 Schematic diagram of disregistry between TiN and FeC_x ($x=3/7, 1/3$).

4.3 PUSHING AND ENGULFMENT BEHAVIOR OF PARTICLES

Descotes et al.[33] found that TiN particles could be engulfed by the solid side at the solid-liquid interface in the solidification process. However, Pervushuin et al.[34] reported that TiN was pushed into the liquid side in molten steel during solidification. In our previous study[22], the local cooling rate and movement velocity of solidification front are confirmed as 0.7 K/s and 3 $\mu\text{m/s}$ by the observation of confocal laser scanning microscope (CLSM), respectively. The changes of temperature, time, and distance are approximately 7 K, 10.6 seconds, and 32 μm , as shown in **Figure 8**. The critical velocity of pushing or engulfment $V_{\text{cr}}=23/R$ (R is the radius for globular particles)[35], when R comes to be 12.5 μm and 2.5 μm (the particles in **Figure 2**), V_{cr} are equal to 1.84 $\mu\text{m/s}$ and 9.2 $\mu\text{m/s}$, respectively. That means the large size TiN inclusion is easier to be engulfed than small size TiN. In the actual process, the local cooling rate is 0.5 to 10 K/s. The higher the local cooling rate is, the faster the solidification front moves, and the more easily the inclusions are engulfed.

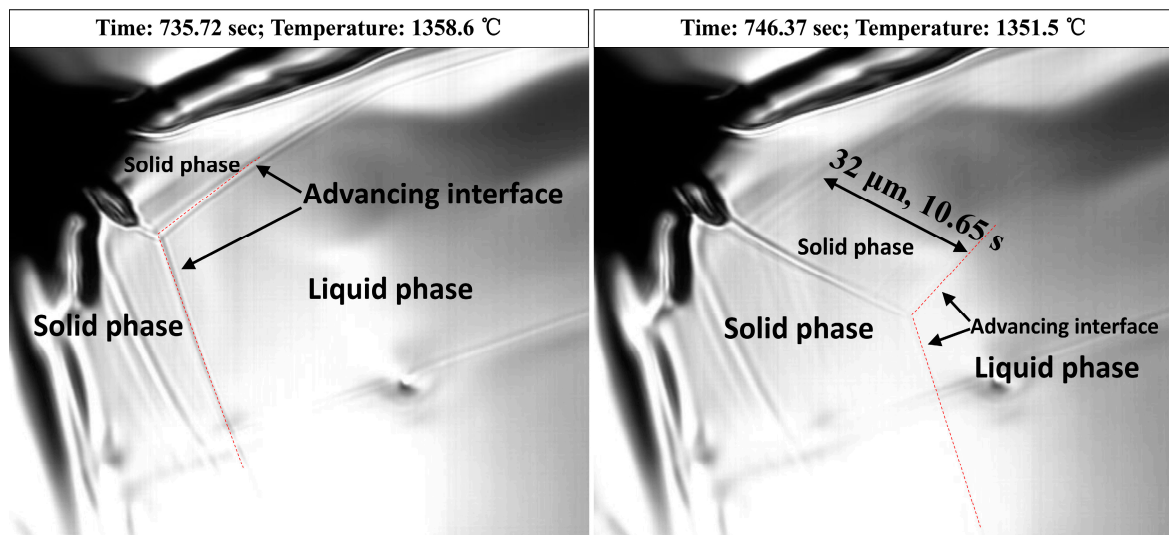


Figure 8 Parameters and distance changes of solidification front in GCr15 bearing steel.

The size of TiN-MC_x is larger than TiN , TiN-MC_x moves more slowly than TiN and is easier to be swallowed by the solidification front. After the engulfment, particles will continue to grow through solid state diffusion, the rate of which will decrease with decreasing temperature. For TiN-MC_x pushed to the liquid phase, elements segregation provides possibility for the growth of MC_x on TiN , TiN-MC_x keeps growing until its size is large enough to be engulfed by the solid phase. The precipitation mechanism of TiN-MC_x in different solidification periods can be confirmed.

- TiN-MC_x with high TiN volume fraction precipitates at the early stage of solidification and has better growth kinetics in the melt. After being engulfed by the solidification front, MC_x grows at a lower rate on the surface of TiN .
- TiN-MC_x with low TiN volume fraction precipitates in the late stage of solidification, and have not enough time to grow to large size. Due to high C concentration and segregation, a large amount of MC_x precipitates on TiN surface. When TiN-MC_x is large enough and engulfed by the solidification front, the volume fraction of MC_x is large to cover TiN particle.

5. CONCLUSION

In this study, TiN-MC_x precipitation mechanism in GCr15 bearing steels were analyzed by combining the experiments of non-aqueous electrolysis, FESEM observation with EDS, and XRD analysis, and the theoretical analysis of thermodynamic and crystallographic analysis, and CLSM observation for pushing and engulfment behavior of particles. The main conclusions can be drawn:

- 244 (1) TiN-MC_x composed of TiN and MC_x, TiN is the effective heterogeneous nucleation site for Fe₇C₃
245 and Fe₃C, in which the MC_x precipitates on the surface of TiN was observed in GCr15 bearing steel .
- 246 (2) MC_x (M = Fe, Cr, Mn) in GCr15 bearing steel smelted by converter is mainly composed of M₃C,
247 M₇C₃, and Cr₃C₂.
- 248 (3) TiN-MC_x with high TiN volume fraction precipitates at the early solidification stage. After being
249 engulfed by the solidification front, MC_x grows at a lower rate on the surface of TiN.
- 250 (4) TiN-MC_x with low TiN volume fraction precipitates in the late solidification stage, and does not have
251 enough time to grow to large size. When the size of TiN-MC_x is large enough and engulfed by the
252 solidification front, the volume fraction of MC_x is large to cover TiN particle because of high C concentration
253 and segregation.

254 **ACKNOWLEDGMENTS**

255 The authors gratefully express their appreciation to National Natural Science Foundation of China (Grant
256 Nos. 51874170 and 51634004) for supporting this work.

257

258 **CONFLICTS OF INTEREST**

259 There are no conflicts to declare.

REFERENCES

- [1] Beswick, J. M.; The effect of chromium in high carbon bearing steels. *Metall. Trans. A* **1987**, 18, 1897-1906, <https://doi.org/10.1007/BF02647019>.
- [2] Du, G.; Li, J.; Wang, Z. B.; Control of carbide precipitation during electrosag remelting-continuous rapid solidification of GCr15 steel. *Metall. Mater. Trans. B* **2017**, 48, 2873-2890, <https://doi.org/10.1007/s11663-017-1089-3>.
- [3] Yang, L.; Cheng, G. G.; Li, S. J.; Zhao, M.; Feng, G. P.; Generation mechanism of TiN inclusion for GCr15SiMn during electrosag remelting process. *ISIJ Int.* **2015**, 55, 1901-1905, <https://doi.org/10.2355/isijinternational.ISIJINT-2015-253>.
- [4] Zhou, D. G.; Fu, J.; Chen, X. C.; Li, J.; Precipitation behavior of TiN in bearing steel. *J. Mater. Sci. Technol.* **2003**, 19, 184-186. <https://doi.org/10.3321/j.issn:1005-0302.2003.02.028>.
- [5] Benz, R.; Elliott, J. F.; and Chipman, J.; Thermodynamics of the carbides in the system Fe-Cr-C. *Metall. Trans.* **1974**, 5, 2235-2240. <https://doi.org/10.1007/BF02643938>.
- [6] Benz, R.; Elliott, J. F.; and Chipman, J.; Thermodynamics of the solid phases in the system Fe-Mn-C. *Metall. Trans.* **1973**, 4, 1975-1986. <https://doi.org/10.1007/BF02665426>.
- [7] Krauss, G.; *Principles of Heat Treatment of Steel*, ASM, Metals Park, OH, **1980**, 222-224.
- [8] Monma, K.; Maruta, R.; Yamamoto, T.; Wakikado, Y.; Role of spheroidized carbides on the fatigue life of bearing steel. *Jp. Inst. Metall. J.* **1968**, 32, 1198-1204. <https://doi.org/10.1007/s12540-012-7002-3>.
- [9] Fu, J.; Zhu, J.; Di, L.; Tong, F.; Liu, D.; Wang, Y.; Study on the precipitation behavior of TiN in the microalloyed steels. *Acta Metall. Sin.* **2000**, 36, 801-804. <https://doi.org/10.3321/j.issn:0412-1961.2000.08.005>.
- [10] Lee, M. H.; Park J. H.; Synergistic effect of nitrogen and refractory material on TiN formation and equiaxed grain structure of ferritic stainless steel. *Metall. Mater. Trans. B* **2018**, 49, 877-893. <https://doi.org/10.1007/s11663-018-1218-7>.
- [11] Park, J. S.; Kim, D. H.; Park, J. H.; TEM characterization of a TiN-MgAl₂O₄ epitaxial interface. *J. Alloys Comp.* **2017**, 695, 476-481. <https://doi.org/10.1016/j.jallcom.2016.11.103>.
- [12] Liu, Y.; Zhang, L. F.; Duan, H. J.; Zhang, Y.; Luo, Y.; Conejo, A. N.; Extraction, thermodynamic analysis, and precipitation mechanism of MnS-TiN complex inclusions in low-sulfur steels. *Metall. Mater. Trans. A* **2016**, 47, 3015-3025. <https://doi.org/10.1007/s11661-016-3463-1>.
- [13] Lee, Y.; Cooman, B. C. D.; TiN/NbC compound particle formation during thin slab direct rolling of

- 290 HSLA steel. *Steel Res. Int.* **2014**, 85, 1158-1172. <https://doi.org/10.1002/srin.201300280>.
- 291 [14] Tian, Q. R.; Wang, G. C.; Shang, D. L.; Lei, H.; Yuan, X. H.; Wang, Q.; Li, J.; Precipitation behaviors of
292 TiN inclusion in GCr15 bearing steel billet. *Metall. Mater. Trans. B* **2018**, 49, 1149-1164.
293 <https://doi.org/10.1007/s11663-018-1230-y>.
- 294 [15] Fang, K. M.; Ni, R. M.; Research on determination of the rare-earth content in metal phases of steel.
295 *Metall. Trans. A* **1986**, 17, 315-323. <https://doi.org/10.1007/BF02643907>.
- 296 [16] Bi, Y.; Karasev, A.; Jönsson, P. G.; Three-dimensional investigations of inclusions in ferroalloys. *Steel Res.*
297 *Int.* **2014**, 85, 659-669. <https://doi.org/10.1002/srin.201300157>.
- 298 [17] Wang, G. C.; Li, S. L.; Ai, X. G.; Zhao, C. M.; Lai, C. B.; Characterization and thermodynamics of
299 Al_2O_3 -MnO-SiO₂ (-MnS) inclusion formation in carbon steel billet. *J. Iron Steel Res. Int.* **2015**, 22, 566-572.
300 [https://doi.org/10.1016/S1006-706X\(15\)30041-8](https://doi.org/10.1016/S1006-706X(15)30041-8).
- 301 [18] Zhang, X. W.; Zhang, L. F.; Yang, W.; Wang, Y.; Liu, Y.; Dong, Y. C.; Characterization of the
302 three-dimensional morphology and formation mechanism of inclusions in linepipe steels. *Metall. Mater. Trans.*
303 *B* **2017**, 48, 701-712. <https://doi.org/10.1007/s11663-016-0833-4>
- 304 [19] Zhang, X. W.; Zhang, L. F.; Yang, W.; Dong, Y. C.; Characterization of MnS particles in heavy rail steels
305 using different methods. *Steel Res. Int.* **2017**, 88, 1600080(1-16). <https://doi.org/10.1002/srin.201600080>.
- 306 [20] Zhang, D.; Shen, P.; Xie, J. B.; An, J. M.; Huang, Z. Z.; Fu, J. X.; A method for observing tridimensional
307 morphology of sulfide inclusions by non-aqueous solution electrolytic etching. *J. Iron Steel Res. Int.* **2019**, 26,
308 275-284, <https://doi.org/10.1007/s42243-018-0142-z>.
- 309 [21] Andersson, J.; A thermodynamic evaluation of the Fe-Cr-C system. *Metallurgical Transactions A* **1988**,
310 19, 627-636. <https://doi.org/10.1007/BF02649276>
- 311 [22] Tian, Q. R.; Wang, G. C.; Shang, D. L.; Lei, H.; Yuan, X. H.; Wang, Q.; Li, J.; In Situ Observation of the
312 Precipitation, Aggregation, and Dissolution Behaviors of TiN Inclusion on the Surface of Liquid GCr15
313 Bearing Steel. *Metall. Mater. Trans. B* **2018**, 49, 3137-3150. <https://doi.org/10.1007/s11663-018-1411-8>.
- 314 [23] Turnbull, D.; Vonnegut, B.; Nucleation catalysis. *Ind. Eng. Chem.* **1952**, 44, 1292-1298.
315 <https://doi.org/10.1021/ie50510a031>.
- 316 [24] Bramfitt, B. L.; The effect of carbide and nitride additions on the heterogeneous nucleation behavior of
317 liquid iron. *Metall. Trans.* **1970**, 1, 1987-1995. <https://doi.org/10.1007/BF02642799>.
- 318 [25] Ding, M. Y.; Yang, Y.; Wu, B. S.; Li, Y. W.; Wang, T. J.; Ma, L. L.; Study on reduction and carburization
319 behaviors of iron-based Fischer-Tropsch synthesis catalyst. *Energy Procedia* **2014**, 61, 2267-2270.

- 320 <https://doi.org/10.1016/j.egypro.2014.12.444>.
- 321 [26] Morniroli, J. P.; Gantois, M.; Etude microstructurale de carbures M₇C₃. *J. Appl. Crystal.* **1983**, 16, 1-10.
- 322 <https://doi.org/10.1107/S0021889883009863>.
- 323 [27] Fruchart, D.; Chaudouet, P.; Fruchart, R.; Rouault, A.; Senateur, J. P.; Etudes structurales de composés de type
- 324 cémentite: Effet de l'hydrogène sur Fe₃C suivi par diffraction neutronique. Spectrométrie Mössbauer sur FeCo 2B
- 325 et Co 3B dopés au ⁵⁷Fe. *J. Solid State Chem.* **1984**, 51, 246-252. [https://doi.org/10.1016/0022-4596\(84\)90340-2](https://doi.org/10.1016/0022-4596(84)90340-2).
- 326 [28] Yang, L.; Cheng, G. G.; Zhao, S. J.; Li, M.; Feng, G. P.; Generation Mechanism of TiN Inclusion for
- 327 GCr15SiMn during Electroslag Remelting Process. *ISIJ Int.* **2015**, 55, 1901-1905.
- 328 <https://doi.org/10.2355/isijinternational.ISIJINT-2015-253>.
- 329 [29] Wang, Y. N.; Yang, J.; Bao, Y. P.; Characteristics of BN Precipitation and Growth During Solidification of
- 330 BN Free-Machining Steel. *Metall. Mater. Trans. B* **2014**, 45, 2269-2278.
- 331 <https://doi.org/10.1007/s11663-014-0146-4>.
- 332 [30] Huang, Y. W.; Long, M. J.; Liu, P.; Chen, D. F.; Chen, H. B.; Gui, L. T.; Liu, T.; Yu, S.; Effects of
- 333 partition coefficients, diffusion coefficients, and solidification paths on microsegregation in Fe-based
- 334 multinary alloy. *Metall. Mater. Trans. B* **2017**, 48, 2504-2515. <https://doi.org/10.1007/s11663-017-1045-2>.
- 335 [31] Miettinen, J.; Thermodynamic-kinetic simulation of constrained dendrite growth in steels, *Metall. Mater.*
- 336 *Trans. B*, **2000**, 31, 365-379. <https://doi.org/10.1007/s11663-000-0055-6>
- 337 [32] Ohnaka, I.; Mathematical Analysis of Solute Redistribution during Solidification with Diffusion in Solid
- 338 Phase. *ISIJ Int.* **1986**, 26, 1045-1051. <https://doi.org/10.2355/isijinternational1966.26.1045>
- 339 [33] Descotes, V.; Bellot, J. P.; Witzke, S.; Jardy, A.; Modeling the Titanium Nitride (TiN) Germination and Growth
- 340 during the Solidification of a Maraging Steel. *Proceedings of the 2013 International Symposium on Liquid Metal*
- 341 *Processing & Casting*, TMS (The Minerals, Metals & Materials Society) **2013**, 201-206.
- 342 https://doi.org/10.1007/978-3-319-48102-9_30
- 343 [34] Pervushin, G.V.; Suito, H.; Precipitation behavior of TiN in Fe-10mass% Ni alloy during solidification and
- 344 isothermal holding at 1400 °C, *ISIJ Int.* 2001, 41, 728-737. <https://doi.org/10.2355/isijinternational.41.728>
- 345 [35] Shibata, H.; Yin, H.; Yoshinaga, S.; Emi, T.; Suzuki, M.; In-situ observation of engulfment and pushing of
- 346 nonmetallic inclusions in steel melt by advancing melt/solid interface. *ISIJ Int.* 1998, 38, 149-156.
- 347 <https://doi.org/10.2355/isijinternational.38.149>